1   **Distributed Fiber Optic Measurements of Strain and Temperature in Long-Span**

2   **Composite Floor Beams with Simple Shear Connections Subject to Compartment Fires**

3   Yanping Zhu[1], Matthew Klegseth[1], Yi Bao[2], Matthew S Hoehler[3], Lisa Choe[3], and Genda Chen[1*]

4   [1] Department of Civil, Architectural and Environmental Engineering, Missouri University of Science and

5   Technology, USA

6   [2] Department of Civil, Environmental and Ocean Engineering, Stevens Institute of Technology, USA

7   [3] National Fire Research Laboratory, National Institute of Standards and Technology, USA

8   **Abstract**

9   This study explores an instrumentation strategy using distributed fiber optic sensors to measure

10   strain and temperature through the concrete volume in large-scale structures. Single-mode optical

11   fibers were deployed in three 12.8 m long steel and concrete composite floor specimens tested

12   under mechanical or combined mechanical and fire loading. The concrete slab in each specimen

13   was instrumented with five strain and temperature fiber optic sensors along the centerline of the

14   slab to determine the variation of the measurands through the depth of the concrete. Two

15   additional fiber optic temperature sensors were arranged in a zigzag pattern at mid-depth in the

16   concrete to map the horizontal spatial temperature distribution across each slab. Pulse pre-pump

17   Brillouin optical time domain analysis (PPP-BOTDA) was used to determine strains and

18   temperatures at thousands of locations at time intervals of a few minutes. Comparisons with

19   co-located strain gauges and theoretical calculations indicate good agreement in overall spatial

20   distribution along the length of the beam tested at ambient temperature, while the fiber optic

21   sensors additionally capture strain fluctuations associated with local geometric variations in the

22   specimen. Strain measurements with the distributed fiber optic sensors at elevated temperatures

23   were unsuccessful. Comparisons with co-located thermocouples show that while the increased

24   spatial resolution provides new insights about temperature phenomena, challenges for local

25   temperature measurements were encountered during this first attempt at application to large-

26   scale specimens.

1. Introduction

Structural response to fires has been widely studied using physical experiments and numerical

models [1,2]. Measured or calculated temperature distributions are often used to evaluate

structural response using coupled thermal-mechanical analysis [3-5]. However, it remains

cumbersome to measure temperature distributions with high spatial resolution in structural

materials such as concrete under fire conditions [6]. Historically, discrete (point) temperatures

have been measured using thermocouples; however, dozens, or even hundreds, of

thermocouples must be placed in the concrete formwork prior to casting to get even a coarse

indication of the horizontal and through-depth temperature variation in concrete during heating for

large structures. This is cost and time intensive. Although infrared cameras provide valuable

information about temperature distribution over large areas, they are not suited for measurements

of temperature variation through the depth of a material and can be susceptible to error caused

by changes in surface conditions as well as the presence of flames in the field of view of the

camera [7].

Fiber optic sensors for measuring temperature have seen increased use in structural fire research

due to their ability to survive harsh environmental conditions [8]. For example, fiber Bragg grating

(FBG) sensors [9] have been used to measure strain and temperature up to approximately

300 °C, the temperature at which traditional gratings are annealed (erased). Huang et al. [10,11]

used long-period fiber grating (LPFG) sensors to measure strain and temperature up to 700 °C.

To extend the temperature range further, regenerated FBG (rFBG) sensors were used by Rinaudo

et al. [12] to record strain and temperature up to 970 °C. Although grating-based sensors can

measure high strain and temperature, they provide measurements only at a single location; i.e.

the location of the gratings. More recently, measurements that are distributed along the length of

53 an optical fiber, without the need for a grating, have become feasible due to developments such

54 as Brillouin optical time domain analysis (BOTDA) and Brillouin optical time domain reflectometry

55 (BOTDR). For example, pulse pre-pump BOTDA (PPP-BOTDA) has been developed with spatial

56 resolution of 2 cm over 500 m of fiber length. Using this emerging technology in structural

57 condition monitoring to measure strain distributions and detect cracks at ambient temperature has

58 been explored [13,14]. PPP-BOTDA technology used for temperature and strain measurement

59 under fire conditions is still limited. Bao et al. [15,16] studied and calibrated temperature-

60 dependent strain and temperature sensitivities of PPP-BOTDA sensors and went on to use the

61 sensors for strain and temperature measurements in simply-supported steel beams under fire

62 conditions [17]. Additionally, Bao et al. [18] studied temperature measurement and damage

63 detection in concrete beams exposed to fire using PPP-BOTDA sensors and the conducted

64 experiments on the deployment of the technique in small (1.2 m × 0.9 m) steel-concrete composite

65 slabs [19]. Their results showed that one single-mode optical fiber can achieve temperature

66 measurements with accuracy better than 12 %, compared to the readings of thermocouples at

67 the same locations.

68

69 In this study, distributed fiber optic sensors (DFOS) were deployed for the first time in full-scale

70 steel-concrete composite floor slabs tested under mechanical loading or combined mechanical

71 and fire loading. Under mechanical loading at ambient temperature, the mid-span strains

72 measured in the concrete slab using PPP-BOTDA were compared with those linearly interpolated

73 or extrapolated from two strain gauges installed in the same cross section. Under combined

74 mechanical loading and fire conditions, the temperatures measured in the concrete slabs using

75 PPP-BOTDA were compared with values linearly interpolated or extrapolated from nearby

76 thermocouples. Due to undocumented uncertainties in temperature measurement that is required

77 to compensate the discrimination of strain measurements, strain data under the combined

78 mechanical and fire conditions are not reported in this paper.

79

2. Distributed Fiber Optic Sensor

2.1 Working principles of PPP-BOTDA

PPP-BOTDA measures temperature and strain changes by relating them to the change in the

refractive index of an optical fiber and the speed of acoustic wave traveling along the optical fiber.

Their relations are associated with the electrostrictive effect of the fiber that tends to compress

materials in the presence of an electrical field. Through electrostriction, the density and thus

refractive index of the optical fiber are modulated when a pump pulse wave and a counter-

propagating continuous probe (Stokes) wave propagate from two ends of the optical fiber and

encounter at various points of the optical fiber. As a result of the light interaction with the molecular

structure of the fiber, an energy exchange with acoustic phonons occurs to form a back-

propagating acoustic wave or a 'traveling grating' in analogy with FBG sensors. At a speed of

sound in the fiber material, the acoustic wave energizes the reflected light power of the pump

wave. The reflected pump wave is downshifted by the frequency difference between the pump

wave and the probe wave due to the Doppler effect, and thus, adds power to the Stokes wave to

be detectable. In this case, the acoustic wave is referred to as stimulated Brillouin scattering [20].

The Brillouin gain can be determined as a function of position by the time-varying probe wave. As

a result, the location of Brillouin frequency shift can be determined.

97

The Brillouin scattering behavior is influenced by the material properties of the fiber, which are in

turn affected by the applied temperature and strain on the fiber creating a sensor. Compared with

the traditional BOTDA, PPP-BOTDA greatly improves the spatial resolution with a pre-pump pulse

by stimulating the phonon before a narrow bandwidth pulse arrives. For silica-based single-mode

optical fibers, the Brillouin frequency v_B typically varies from 9 GHz to 13 GHz for light

wavelengths of 1.3 μm to 1.6 μm and can be calculated by Equation (1):

$$v_B = \frac{2v_0}{C}nV_a \tag{1}$$

104   where v_0 denotes the frequency of an incipient light wave, n represents the refractive index of the

105   optic fiber, V_a represents the speed of an acoustic wave in the fiber, and C represents the speed

106   of light in a vacuum, which is equal to 3.0×10^8 m/s. The speed of the acoustic wave V_a in the

107   optical fiber is given by [17]:

$$V_a = \sqrt{\frac{(1-\mu)E}{(1+\mu)(1-2\mu)\rho}} \tag{2}$$

108   where μ, ρ, and E represent the Poisson's ratio, density and Young's modulus of the optic fiber,

109   respectively.

110

111   The density and refractive index are affected by both strain (ε) and temperature (T), while the

112   Young's modulus and Poisson's ratio are affected by temperature only. Therefore, strain and

113   temperature changes in the optical fiber cause a shift in the Brillouin frequency. For a change in

114   strain and temperature from reference values obtained during calibration, the Brillouin frequency

115   shift (Δv_B) can be expressed as:

$$\Delta v_B = C_\varepsilon \Delta \varepsilon + C_T \Delta T \tag{3}$$

116   where C_ε and C_T represent the strain and temperature sensitivity coefficients, respectively.

117

118   ***2.2 Fiber optic sensor calibration***

119   Telecommunication-grade, single-mode optical fiber cable was used as a distributed temperature

120   sensor. The temperature sensor (Figure 1) has a polymer outer sheath (diameter: 3 mm), a layer

121   of aramid yarn, a tight polymer buffer (diameter: 880 µm), a polymer outer coating (outer diameter:

122   242 µm), a polymer inner coating (outer diameter: 190 µm), a silica glass cladding (outer diameter:

123   125 µm), and a silica glass core (diameter: 8.2 µm). The polymer of the inner and outer coatings

124   as well as the tight buffer is composed of mixtures of monomers, oligomers, photoinitiators, and

125   additives. The outer sheath protects the temperature sensor from abrasion. The polymer buffer

126   and coatings protected the glass from mechanical impact and from undesired environmental

127   exposure. The aramid yarn significantly reduces the transfer of axial strain from the outer sheath

128   to the measurement fiber at a room temperature (approximately 22 °C) based on the tests of

129   1.2 m × 0.9 m steel-concrete composite slabs [19]. However, the efficacy of the yarn to eliminate

130   axial strain over long distances (> 4 m with multiple 180° turns) at elevated temperature (> 22 °C)

131   and embedded in concrete where the fiber path is torturous, was not verified. The cost of the

132   sensor cable was approximately $0.40 USD per m. A similar optical fiber without the outer sheath

133   and aramid yarn was used as a distributed strain sensor; i.e., the concrete was in direct contact

134   with the polymer buffer allowing transfer of mechanical strain from the concrete to the optical fiber

135   core. It is assumed that sheathing, buffer and coatings have a glass transition temperature of less

136   than 180 °C. The silica glass core and cladding can sustain temperatures above 1000 °C.

137

138   For an optical fiber that is free of strain change, the Brillouin frequency shift is dependent on

139   temperature change only. However, this relationship is nonlinear when a large change in

140   temperature occurs. Based on the results in [15], [16], [18], and [21], a relationship between the

141   temperature sensitivity coefficient and temperature for the investigated fiber optic temperature

142   sensors is given in Equation (4). It is noted that any transient reduction of temperature when the

143   sensor coatings melt is neglected. When both strain and temperature change, an additional fiber

144   that is (approximately) free of strain can be incorporated for temperature compensation. Equation

145   (3) can then be rearranged to find the change in strain after the strain sensitivity coefficient C_ε has

146   been determined empirically with temperature up to 800 ℃ as shown in Equation (5). This is the

147   strain sensitivity of bare optical fiber sensors, which should not be applied for strain sensing at

148   elevated temperature unless the behavior of strain transfer between the fiber and its surrounding

149 base material (concrete) is well understood and taken into account. The temperature unit in

150 equations (4) and (5) is °C.

$$C_T = -6.928 \times 10^{-7}T + 1.110 \times 10^{-3} \tag{4}$$

$$C_\varepsilon = -1.228 \times 10^{-5}T + 4.97 \times 10^{-2} \tag{5}$$

151

152 **3. Experimental program**

153 *3.1 Test specimens*

154 Three 12.8 m long composite floor beams that were part of a larger study of the performance of

155 composite construction in fire [22] were instrumented with distributed fiber optic sensors. These

156 unique large-scale composite specimen experiments were leveraged to explore the advantages

157 and disadvantages of distributed fiber optic sensing technology compared to conventional

158 sensors. The specimens were designed with double angle end (shear) connections in accordance

159 with current codes and standards [23, 24] in the United States. The first beam with no slab end

160 continuity as a baseline to the other beams, designated as CB-DA-AMB, was tested to failure

161 under mechanical loading at ambient temperature to understand its ultimate strength. Identical to

162 the first beam, the second specimen, designated as CB-DA, was tested to failure under combined

163 mechanical loading and fire. The third beam with slab end continuity, designated as CB-DA-SC,

164 was tested to failure under combined mechanical loading and fire. Design details for the

165 specimens are presented in [25, 26]. The magnitude of mechanical loading applied on the second

166 and third beams corresponded to 45 % of the ultimate moment capacity of the first beam [27].

167 The fire was generated using natural gas burners with a maximum total heat release rate of 4 MW.

168

169 Figures 2(a) and (b) give the end connection with double angles and slab continuity (using four

170 no. 4 reinforcing bars), and the cross section of the CB-DA-SC specimen, respectively. A 1.83 m

171 wide by 12.8 m long lightweight aggregate concrete slab with polypropylene microfibers was cast

172 on 20-gauge profiled metal decking above a W18×35 steel beam. Headed studs (19 mm shaft

173   diameter) were welded to the steel beam with a spacing of 305 mm. The degree of composite

174   action between the concrete and the beam achieved by the studs was approximately equal to

175   82 % of the ambient yield strength of the steel cross section (W18×35). Welded wire fabric (6×6

176   W1.4×W1.4) was embedded at 42 mm below the top surface of the concrete to satisfy minimum

177   shrinkage and temperature cracking control requirements in Steel Deck Institute Standard C-2011

178   [28]. The bottom flange of the steel beam was coped at both ends (Figure 2(a)) to accommodate

179   the double angles during construction. For CB-DA-SC, four additional no. 4 steel reinforcing bars

180   were embedded in the negative bending moment region near the end supports and anchored to

181   a hollow steel section to simulate the slab continuity. The steel beam was coated with sprayed

182   fire resistive materials (SFRM) to achieve a 2-hour fire resistance rating along the member and a

183   3-hour fire rating at the connections.

184

185   ***3.2 Material properties***

186   A full description of the specimen material properties is available in [22]. Select properties relevant

187   to the distributed fiber optic sensors are provided here. All material properties were determined in

188   accordance with the relevant ASTM standards [29–37]. Polypropylene microfiber reinforced

189   lightweight aggregate concrete with a water-to-binder ratio of 0.46 was used for the test

190   specimens. The sand used was a natural product comprised of silica grains. High-range water

191   reducer was added to achieve a design slump of 216 mm and limit the required mechanical

192   vibration of the concrete. This was intended to prevent breakage of the distributed optical fiber

193   sensors during casting. The polypropylene microfibers (25 mm long and 40 μm in diameter at a

194   dosage of 2.37 kg/m^3) were used to reduce the likelihood of spalling of the concrete under fire

195   conditions [38]. The mean 28-day concrete cylinder compressive strength was 45.4 MPa. After

196   curing for 6 months, internal relative humidity in the concrete dropped to about 80 %. The fire

197   experiments were conducted about 12 months after the concrete placement. For the W18×35

198   beams, the measured yield and ultimate tensile strengths were 360 MPa and 470 MPa,

199 respectively. The modulus of elasticity of the steel beams was 203 GPa. The measured ultimate

200 strength for bolts, shear studs, and welded wire fabrics was 960 MPa, 510 MPa, and 760 MPa,

201 respectively.

202

203 *3.3 Test setup and instrumentation*

204 The test setup is shown in Figure 3. The test specimen, for which the soffit of the slab was elevated

205 3.8 m above the laboratory floor, was attached to longitudinally braced W12x106 steel columns

206 at the west and east ends. Six equally distributed point loads were applied to the specimen along

207 its centerline using three pairs of servo-hydraulically controlled actuators attached to the ends of

208 loading beams coupled with triangular loading trusses. To confine the fire below the specimen,

209 enclosure walls were constructed below the specimen using cold-formed steel framing and sheet

210 steel. The fire-exposed wall surfaces were protected with two layers of 25 mm thick ceramic fiber

211 blankets. Three natural gas diffusion burners with servo-controlled gas mass flow were arranged

212 along the center of the compartment floor and were used to heat the specimen. This setup

213 replicated a 1.83 m wide strip of a building around the beam-column centerline for which a realistic

214 fire and design gravity load could be simultaneously applied at full-scale.

215

216 Three strain distributed fiber optic sensors (L-DFOS) were placed longitudinally along the

217 centerline of the beam at approximately 32 mm, 51 mm, and 70 mm below the top surface of the

218 concrete as shown in Figure 4(a). Two temperature fiber optic cables were co-located with the

219 top and bottom strain sensors. The longitudinal sensors were taped to thin wires spanned from

220 end-to-end in the slab so that they could maintain their position during casting of the concrete. As

221 shown in the excerpt of Figure 4(a), all five L-DFOS were collected and turned by 90° to an exit

222 point for data acquisition during tests. Additionally, two transverse distributed fiber optic sensors

223 (T-DFOS) were deployed in a zig-zag pattern on the weld wire fabric (reinforcement) to measure

224 the temperature distribution in the concrete slab approximately 41 mm from its top surface (Figure

9

225 4(b)). Since the top L-DFOS was placed prior to the installation of the T-DFOS, the transverse

226 fibers were raised for about 10 mm in elevation near the centerline of the specimen as detailed in

227 the insert of Figure 4(b). Several of the sensors were spliced together in series outside of the

228 concrete so their data could be acquired simultaneously on a single analyzer. The strain and

229 temperature distributed fiber optic sensors have a 95 % confidence interval of $\pm$ 1.63 % and

230 $\pm$ 3.66 %, respectively, based on the coefficient of variation of nine adjacent measurement points.

231

232 To validate the spatially-distributed temperature measurements from the distributed fiber optic

233 sensors, six glass-sheathed 24-gauge Type K thermocouples (TC) were deployed on the welded

234 wire fabric and top of the metal decking at each of the eight sections (x = 1 through 8) as shown

235 in Figure 5. At each section, two thermocouples (TCx-7 and TCx-8) were installed right above the

236 steel beam in centerline, two (TCx-2 and TCx-3) were located at 46 cm north of the beam

237 centerline and two (TCx-17 and TCx-18) at 46 cm south of the beam centerline. At mid-span

238 section of the CB-DA-AMB specimen, two strain gauges were deployed in the concrete slab: one

239 on the top surface and the other at 4.1 cm below in the concrete. Additional strain gauges were

240 installed at the top and bottom flanges as well as the mid-height web of the steel beam.

241

242 The location where each optical fiber run entered and exited the concrete as detected by the PPP-

243 BOTDA analyzer was determined immediately prior the fire testing. This was done by placing an

244 ice cube on points of interest on the fiber which provided a measurable localized temperature

245 decrease. The position of the fibers inside the concrete had been mapped prior to concrete

246 casting.

247

248 *3.4 Test protocols*

249 To establish the baseline specimen behavior and understand the performance of strain DFOS at

250 ambient temperature, the CB-DA-AMB specimen with no slab continuity was tested to failure

251 under six point-loads as positioned in Figure 3. Figure 6 presents the load-deflection curve at mid-

252 span, beam rotations at two ends, deflection curves, and strain distribution in mid-span cross

253 section during the first cycle of point loading up to P_{max} equal to 63 kN (maximum load). It can be

254 seen from Figure 6 that both the end rotations and the deflection curves indicated more severe

255 displacement on the west end of the specimen even under six well-controlled point loads

256 symmetric about the mid-span. Based on two measurements in the concrete slab and two

257 measurements in the steel beam, the strain distribution in the cross section at mid-span shows

258 discontinuity at the slab-beam interface, which is indicative of partial slip particularly at a load of

259 $0.75P_{max}$ or higher. At $0.25P_{max}$, the strain discontinuity or slip at the interface is negligible. The

260 neutral axis of the concrete cross section under various load levels ranged from 125 mm to

261 155 mm from the top surface of the concrete slab and near the top flange of the steel beam at

262 mid-span.

263

264 The experimental protocol used for CB-DA and CB-DA-SC specimens was as follows: (1) a total

265 mechanical load of 106 kN (17.7 kN/point load or 45 % of the ultimate moment) was applied and

266 held constant at ambient temperature, (2) the heat release rate in the compartment under the

267 beam was increased to 4 MW over a period of 15 min and held constant, and (3) a cooling phase

268 was initiated by linearly decreasing the heat release rate over 30 min. The applied total

269 mechanical loading and compartment upper layer gas temperature histories for the specimens

270 instrumented with distributed fiber optic sensors are shown in Figure 7. Note that the applied point

271 load (17.7 kN) is slightly higher than $0.25P_{max}$ = 15.75 kN in Figure 6.

272

273 **4. Results and discussion**

274 ***4.1 Strain distribution from longitudinal DFOS at ambient temperature***

275 Typical fiber optic strain measurements along the centerline of specimen CB-DA-AMB at ambient

276 temperature under applied mechanical loads of 11 kN, 22 kN, and 44 kN are presented in Figure

277   8. To account for potential misalignment of the position of fibers, a moving average of nine points

278   was applied to increase the effective sensor gauge length to 10 cm, which was deemed to be

279   appropriate for the investigated trapezoidal decking dimensions. Idealized strain predictions

280   based on simple elastic analysis with the neutral axis located at 135 mm from the top surface of

281   the thin concrete slab and ignoring slip within the cross section are also shown in Figure 8 at the

282   corresponding depths. Because six point-loads were applied on the simply supported beam, the

283   elastic strain distribution follows a piecewise linear line that resembles a parabolic curve. The

284   theoretical predictions and the measured strain distributions from the DFOS agree reasonably

285   well in terms of overall shape. Figure 8 also shows measurements from the resistance-based

286   strain gauges at mid-span (with required linear interpolations or extrapolations), which closely

287   resemble the DFOS strains at these locations. The advantage of the DFOS measurements are

288   that they provide information about the continuous strain distribution along the length of the

289   specimen whereas the conventional strain gauges provide information only at single points. The

290   causes of the local variations in the DFOS strain in this large test specimen may be ascribed to

291   local strain concentrations around the headed studs, spatial variations of the slab depth in

292   conformance with the metal decking, concrete material heterogeneity, or local variation in the

293   optical fiber path. The authors believe however that many of the variations are associated with

294   the periodic change of the headed studs and slab depth as evidenced by the fact that peaks

295   appear at the same locations in all three fibers with varying amplitude. Note that the longitudinal

296   DFOS readings at the ends of the specimen (before Section 1 and after Section 8 as indicated in

297   Figure 5(a)) are misrepresentative because the longitudinal sensors at different elevations were

298   bundled together during a 90° turn as shown in the insert of Figure 4(a) and thus not considered

299   in the following analysis both for strain and temperature measurements.

300

301   *4.2 Temperature distribution from longitudinal DFOS in fire conditions*

302   Figure 9 compares concrete temperatures measured at different times from the longitudinal DFOS

303   and thermocouples deployed along the centerline of the CB-DA specimen that was tested under

304   simultaneous mechanical and fire loads. The fiber optic temperature sensors were located 32 mm

305   (Top) and 70 mm (Bottom) below the top surface of the concrete slab. Their closest

306   thermocouples were positioned at 41 mm and 82 mm from the top surface of the slab. Therefore,

307   the thermocouple temperatures were linearly interpolated or extrapolated to obtain the

308   temperatures at the locations of the fiber optic sensors for comparison.

309

310   The thermocouple temperatures in Figure 9(a, b) at a given time follow a roughly horizontal line

311   along the length of the specimen; except at Section 4 (Bottom) and Section 6 (Top and Bottom)

312   where temperatures jump suddenly to 100 °C by 20 min into the test. This is more clearly

313   illustrated by Figure 10, which shows the complete thermocouple temperature-time histories; refer

314   to Figure 5 for thermocouple locations. As moisture is driven out of the concrete during heating

315   (desiccation), it will maintain a temperature of 100 °C as the water is vaporized. This results in a

316   plateau in the time versus temperature curve until the water is driven off. A temperature plateau

317   at 100 °C is also visible in many thermocouples to the north and south of the centerline, however,

318   the rise to 100 °C is gradual. Thus while amplitude of 100 °C at Sections 4 and 6 is likely caused

319   by water vaporization, the rise time is clearly erroneous – possibly caused by multi unintended

320   junctions in the lead wires – and these data are disregarded in the subsequent analysis. It is also

321   noted from Figure 10 that along the centerline of the beam specimen, the heating of the concrete

322   is slower than to the north and south due to the thermal shadowing from the beam underneath.

323

324   The DFOS also exhibits an overall horizontal temperature distribution along the specimen,

325   particularly the top temperature sensor; however, the curves show prominent local temperature

326   peaks. The large, non-periodic singular peaks in the DFOS temperature are likely associated with

327   the formation of cracks in the concrete. There are also smaller amplitude periodic variations visible

328   in the DFOS readings. Due to the trapezoidal shape of the metal decking, the concrete cover to

329   the bottom optical fiber from the fire varies from 13 cm to 89 cm over a length of 30.5 cm (refer to

330   Figure 2(a)). This results in periodic local temperature fluctuation along the length of the

331   composite beam as can be seen most clearly in the data extracted from Figure 9(b) between

332   2.44 m and 5.49 m shown in Figure 9(c). The local maxima represent the locations of the thinner

333   concrete cover (13 cm) to the heated surface of the slab; however, this behavior is complicated

334   by the presence of the cracks in the concrete which cause prominent singular temperature

335   variations. This amplitude fluctuation at 30.5 cm spacing is most pronounced at 70 min, i.e., during

336   the controlled cooling phase of a fire, and then gradually disappears.

337

338   The minimum, average, and maximum section-by-section differences in the temperature readings

339   between the DFOS and thermocouples are compared in Table 1 at the locations of

340   thermocouples. Any difference below 20% in Table 1 are highlighted in bold face. The

341   temperature difference at a single location ranges from zero to 232 % with an average value less

342   than 26 % for specimen CB-DA except at the peak of gas temperature right after mechanical

343   unloading. The reasons for the large maximum differences may include variation in the position

344   of the measurement locations in the concrete (up to several cm), heat transfer (or cooling) along

345   the fiber and sheathing, required acquisition time (e.g., 2 min) to sweep the range of Brillouin

346   frequency, and the inherent uncertainty of the two measurement techniques.

347

348   Figure 11 shows the test data for the CB-DA-SC specimen. Like the CB-DA specimen, the unique

349   information provided by the DFOS that is not apparent in the thermocouple data is the local spatial

350   variation of temperature. A prominent example of this can be seen between Section 3 and Section

351   6. There are indications of significant cracks formed at the bottom of concrete slab near Sections

352   3 and 4, and at the top of the slab near Sections 5 and 6. Once the concrete has been fully

353 desiccated at the sensor location after 70 min of burning, the local temperature variation at the

354 cracks becomes less prominent as shown for the lower fiber in Figure 11(b). Note that minor

355 cracks likely occur between Section 5 and 8 closing to the lower fiber. As with specimen CB-DA,

356 low-amplitude periodic temperature variations are visible along the optical fiber between 7.67 m

357 and 10.72 m resulting from the varying concrete cover thickness to the heat source (Figure 11(c)).

358

359 Unlike the CB-DA specimen, both the thermocouple data and the DFOS data of the CB-DA-SC

360 specimen indicate a temperature rise near the ends of the slab compared to the middle of the

361 slab. This is due to the pronounced cracking in these portions of the slab, which provided

362 additional paths for moisture transport out of the concrete. For the CB-DA specimen, the end

363 temperature rise is not prominent because the heating of the slab was stopped 40 min after burner

364 ignition before the moisture had been driven out of the concrete at the sensor locations. For

365 specimen CB-DA-SC, the end continuity provided by four reinforcing bars in this specimen and

366 longer heating time, leading to larger bending deformation of the specimen, led to multiple large

367 cracks observed at the top side of concrete slab as shown in Figure 12(a). It was observed during

368 the experiment that the concrete slab above the west angle connection cracked at 43 min, and

369 released black smoke on top of concrete at 48 min and visible flames at 54 min. The concrete

370 slab near the east support cracked at 50 min, and released black smoke at 52 min and visible

371 flames at 60 min. This is further evidenced by the concrete discoloration along the crack surface

372 seen in Figure 12(b). These observations are supported by the measured tensile forces in the

373 reinforcing bars as presented in Figure 13. Thus, the thermocouple readings at the end portion of

374 the concrete slab are indicative of flame/hot air temperature through penetrated cracks, resulting

375 in a temperature difference of over 200 °C between two closely spaced thermocouples (e.g., TCx-

376 7 and TCx-8) at 65 min. as shown in Figure 10. As a result, thermocouple data at Sections 1 and

377 8 are not used for comparison with the DFOS data in the following analysis.

378

379   The combined effect of the opening of metal deck seams and multiple penetrated concrete cracks

380   caused the end temperature rise. The heat radiation through metal decking and heat convection

381   through seam opening and concrete cracks are combined to create the complicated mechanical

382   and thermal field in the CB-DA-SC specimen. While the thermocouple measurement indicates

383   cooling of the slab between 90 min and 120 min at the ends of the slab as a result of completing

384   moisture evaporation, the DFOS indicates continued increase in temperatures. This inconsistency

385   is likely attributed to the unintended strain induced along the distributed temperature sensor by

386   multiple cracks (both top and bottom of the concreate slab) in addition to other factors as

387   discussed for the CB-DA specimen. As shown in Table 1, the temperature difference between the

388   two methods ranges from zero to 130 % at single sections with an average value of less than 59

389   % in the CB-DA-SC specimen.

390

391   *4.3 Temperature distribution from transverse DFOS in fire conditions*

392   Figures 14(a) and 14(b) show measured temperature distributions at 90 min after ignition in the

393   slabs of CB-DA and CB-DA-SC, respectively. The vertical axis represents the width of the slab

394   and the horizontal axis represents the length of the slab (not to scale). The measured

395   temperatures were calculated from the results of two transverse fiber optic sensors (T-DFOS) as

396   shown in Figure 4(b) for CB-DA, and the second T-DFOS only for CB-DA-SC (the first T-DFOS

397   was broken prior to testing). Figure 14 shows some regionally periodic temperature variations due

398   to the varying slab thickness although the transverse fibers were deployed with a varying

399   longitudinal spacing of 15 cm to 45 cm, which is insufficient to resolve the full resolution of spatial

400   periodicity (30.5 cm) in the concrete slab. It is notable that the T-DFOS data for specimen CB-

401   DA-SC does not indicate a temperature increase near the end of the slab at the centerline of the

402   beam as suggested by the L-DFOS data. This is because the cracks at the ends of the slab did

403   not penetrate through the transverse fibers on the north and south side of the centerline as

404   evidenced in Figure 12(a).

405

406   Figures 15(a) and Figure 15(b) compare the T-DFOS and thermocouple data for the slabs of CB-

407   DA and CB-DA-SC specimens, respectively. In each figure, the temperatures along the centerline,

408   north and south sides of the beam are presented. In general, the concrete temperature at the

409   centerline is lower than that on the side lines due to the thermal shading effect of the steel beam

410   and the temperatures on the north and south sides are roughly symmetric. This agrees with the

411   observation from the thermocouples presented in Figure 10. The quantitative section-by-section

412   comparison between the T-DFOS and thermocouple data is summarized in Table 2. For the CB-

413   DA specimen, the average difference is within 19 % along the north and south lines and 29 %

414   along the centerline (thermocouple data at Sections 4 and 6 are excluded as discussed when

415   compared with the L-DFOS readings). The maximum difference at single sections is 54 %. For

416   the CB-DA-SC specimen, the average difference is within 35 % (thermocouple data at Sections

417   1 and 8 are excluded). The maximum difference at single sections is 59 % along the north and

418   south lines and 78 % along the centerline.

419

420   **5 Conclusions**

421   This study applied pulse pre-pumped Brillouin optical time domain analysis along a single-mode

422   optic fiber for strain and temperature measurements in large-scale concrete composite structures.

423   For strain measurements at ambient temperature, the high spatial resolution in the concrete slab

424   with a profile decking above a steel beam is promising to shed light on the presence of shear

425   studs and cross-section thickness variations. The measured strains at mid-span of the

426   CB-DA-AMB specimen compared well with the linear interpolation and extrapolation of readings

427   from strain gauges in the concrete slab. For temperature measurements under simultaneous

428   mechanical loading and fire, the effectiveness of distributed fiber optic sensors was verified

429   against thermocouples. Unlike thermocouples, unique peaks relevant to the concrete cracks and

17

430   regionally periodic temperature variation due to the varying slab thickness can be captured by the

431   distributed sensors under high temperatures.

432

433   From longitudinal distributed fiber optic sensors, the measured temperature increases with time

434   from ignition as observed from co-located thermocouples. For the CB-DA specimen with no end

435   slab continuity, the average temperatures from the two measurement techniques differ by less

436   than 26 % except at the peak of gas temperature right after mechanical unloading. Most

437   distributed sensor readings (averaged over 10 cm in length) are lower than those from

438   thermocouples (point measurement). For the CB-DA-SC specimen with end slab continuity, the

439   average temperatures from the two techniques differ by 59 %. The different measurement

440   accuracies between the two specimens mainly result from the prolonged loading and fire duration

441   as well as end slab continuity, causing complex degradation (damage) near two ends of the

442   specimens under combined mechanical and fire conditions.

443

444   From transverse distributed fiber optic sensors, the average difference in measured temperatures

445   between the fiber optic sensors and thermocouples is within 19 % along sidelines and 29 % along

446   centerline of the CB-DA specimen. For the CB-DA-SC specimen, the average difference is within

447   35 %.

448

449   The above comparisons between optical sensors and their adjacent thermocouples are made at

450   individual cross sections of the tested floor beam. They are sensitive to any misalignment of the

451   two types of sensors. Nevertheless, challenges still exist to uncouple the effects of temperature

452   and strain when multiple cracks penetrate through distributed fiber optic sensors deployed in long

453   distances. Future studies will be directed to further understand the bond between distributed strain

454   sensors and concrete under high temperatures, and the local anchor effect on the performance

455 of distributed temperature sensors when deployed with a zigzag pattern including multiple 180°

456 turns.

457

458 **Acknowledgements**

465

466 **Author Statements**

467 Yanping Zhu: Formal Analysis, Writing – Original Draft, Visualization, Methodology. Matthew

468 Klegseth: Investigation, Data Curation, Writing- Original Draft. Yi Bao: Conceptualization,

469 Methodology. Matthew Hoehler: Validation, Investigation, Writing – Review & Editing. Lisa Choe:

470 Methodology, Project Administration. Genda Chen: Conceptualization, Writing – Review &

471 Editing, Supervision, Funding Acquisition.

472

473 **References**

474 [1].   L. Bisby, J. Gales, C. Maluk, A contemporary review of large-scale non-standard structural

475   fire testing, Fire Sci. Rev. 2 (2013) 1. doi:10.1186/2193-0414-2-1.

476 [2].   J.M. Franssen, T. Gernay, Modeling structures in fire with SAFIR®: Theoretical

477   background and capabilities, J. Struct. Fire Eng. 8 (2017) 300–323. doi:10.1108/JSFE-07-

478   2016-0010.

479 [3].   V.K.R. Kodur, M. Dwaikat, A numerical model for predicting the fire resistance of

480   reinforced   concrete   beams,   Cem.   Concr.   Compos.   30   (2008)   431–443.

481   doi:10.1016/j.cemconcomp.2007.08.012.

482   [4].   A.E. Jeffers, E.D. Sotelino, Fiber heat transfer element for modeling the thermal response

483   of structures in fire, J. Struct. Eng. 135 (2009) 1191–1200. doi:10.1061/(ASCE)ST.1943-

484   541X.0000043.

485   [5].   L. Jiang, A. Usmani, Towards scenario fires – modelling structural response to fire using

486   an integrated computational tool, Adv. Struct. Eng. 21 (2018) 2056–2067.

487   doi:10.1177/1369433218765832.

488   [6].   J.C. Yang, M.F. Bundy, J.L. Gross, A.P. Hamins, F.H. Sadek, A. Raghunathan,

489   International R and D Roadmap for Fire Resistance of Structures Summary of NIST/CIB

490   Workshop (NIST SP 1188), (2015). doi:10.6028/NIST.SP.1188.

491   [7].   M.S. Hoehler, On the development of a transparent enclosure for 360° video cameras to

492   observe severe fires in situ, Fire Saf. J. (2020) 103024. doi:10.1016/j.firesaf.2020.103024.

493   [8].   Y. Bao, Y. Huang, M.S. Hoehler, and G. Chen, Review of fiber optic sensors for structural

494   fire engineering, Sensors 19(2019) 877. doi.org/10.3390/s19040877.

495   [9].   B. Zhang, M. Kahrizi, High-temperature resistance fiber Bragg grating, Sensors 7 (2007)

496   586–591.

497   [10].   Y. Huang, X. Fang, W.J. Bevans, Z. Zhou, H. Xiao, G. Chen, Large-strain optical fiber

498   sensing and real-time FEM updating of steel structures under the high temperature effect,

499   Smart Mater. Struct. 22 (2013). doi:10.1088/0964-1726/22/1/015016.

500   [11].   Y. Huang, Z. Zhou, Y. Zhang, G. Chen, H. Xiao, A temperature self-compensated LPFG

501   sensor for large strain measurements at high temperature, IEEE Trans. Instrum. Meas. 59

502   (2010) 2997–3004. doi:10.1109/TIM.2010.2047065.

503   [12].   P. Rinaudo, B. Torres, I. Paya-Zaforteza, P.A. Calderón, S. Sales, Evaluation of new

504   regenerated fiber Bragg grating high-temperature sensors in an ISO 834 fire test, Fire Saf.

505   J. 71 (2015) 332–339. doi:10.1016/j.firesaf.2014.11.024.

506   [13].   Y. Bao, M. Valipour, W. Meng, K.H. Khayat, G. Chen, Distributed fiber optic sensor-

507   enhanced detection and prediction of shrinkage-induced delamination of ultra-high-

508   performance concrete overlay, Smart Mater. Struct. 26 (2017) 085009. doi:10.1088/1361-

509   665X/aa71f4.

510 [14]. Y. Bao, W. Meng, Y. Chen, G. Chen, K.H. Khayat, Measuring mortar shrinkage and

511   cracking by pulse pre-pump Brillouin optical time domain analysis with a single optical

512   fiber, Mater. Lett. 145 (2015) 344–346. doi:10.1016/j.matlet.2015.01.140.

513 [15]. Y. Bao, G. Chen, Temperature-dependent strain and temperature sensitivities of fused

514   silica single mode fiber sensors with pulse pre-pump Brillouin optical time domain analysis,

515   Meas. Sci. Technol. 27 (2016). doi:10.1088/0957-0233/27/6/065101.

516 [16]. Y. Bao, G. Chen, High-temperature measurement with Brillouin optical time domain

517   analysis of an annealed fused-silica single-mode fiber, Opt. Lett. 41 (2016) 3177.

518   doi:10.1364/ol.41.003177.

519 [17]. Y. Bao, Y. Chen, M.S. Hoehler, C.M. Smith, M. Bundy, G. Chen, Experimental analysis of

520   steel beams subjected to fire enhanced by Brillouin scattering-based fiber optic sensor

521   data, J. Struct. Eng. 143 (2016) 04016143. doi:10.1061/(asce)st.1943-541x.0001617.

522 [18]. Y. Bao, M. Hoehler, C.M. Smith, G. Chen, Temperature measurement and damage

523   detection in concrete beams exposed to fire using PPP-BOTDA based fiber optic sensors,

524   Smart Mater. & Struct. 26 (10) (2017), 105034. doi:10.1088/1361-665X/aa89a9.

525 [19]. Y. Bao, M.S. Hoehler, C.M. Smith, M. Bundy, and G. Chen, Measuring three-dimensional

526   temperature distributions in steel-concrete composite slabs subjected to fire using

527   distributed fiber optic sensors, Sensors, 20(2020), 5518. doi:10.3390/s20195518.

528 [20]. K. Kishida and C.H. Li, Pulse pre-pump-BOTDA technology for new generation of

529   distributed strain measuring system, Proc. 2005 Struct. Health Monit. & Intelligent Infra.

530   Conf., Shenzhen, China.

531 [21]. Y. Bao, M. Hoehler, C.M. Smith, G. Chen, Measuring temperature distribution in steel-

532   concrete composite slabs subjected to fire using Brillouin scattering based distributed fiber

533   optic sensors, Proc. 2019 Struct. Health. Monit. & Intelligent Infra. Conf., St. Louis, USA.

534 [22]. L. Choe, S. Ramesh, W. Grosshandler, M. Hoehler, M. Seif, J. Gross, M. Bundy, Behavior

535   and limit states of long-span composite floor beams with simple shear connections subject

536   to compartment fires : experimental evaluation, ASCE J. Struct. Eng. 146 (2020) 1–14.

537   https://doi.org/10.1061/(ASCE)ST.1943-541X.0002627.

538 [23]. ANSI/AISC-360 (2016). Specification for Structural Steel Buildings. American Institute of

539   Steel Construction, Chicago, Illinois.

540 [24]. ASCE/SEI 7 (2016). Minimum Design Loads for Buildings and Other Structures. American

541   Society of Civil Engineers, Reston, Virginia.

542 [25]. S. Ramesh, L.Y. Choe, M.S. Seif, M.S. Hoehler, W.L. Grosshandler, A. Sauca, M.F.

543   Bundy, W.E. Luecke, Y. Bao, M. Klegseth, G. Chen, J. Reilly, B. Glisic. Compartment Fire

544   Experiments on Long-Span Composite-Beams with Simple Shear Connections Part 1:

545   Experiment Design and Beam Behavior at Ambient Temperature. NIST Technical Note

546   2054, Gaithersburg, MD, 2019 https://doi.org/10.6028/NIST.TN.2054.

547 [26]. L. Choe, S. Ramesh, M.S. Hoehler, M.S. Seif, M. Bundy, J. Reilly, B. Glisic. Compartment

548   Fire Experiments on Long-Span Composite-Beams with Simple Shear Connections Part

549   2: Test Results. NIST Technical Note 2055, Gaithersburg, MD, 2019

550   https://doi.org/10.6028/NIST.TN.2055.

551 [27]. L. Choe, S. Ramesh, M. Hoehler, J. Gross, Experimental study on long-span composite

552   floor beams subject to fire: baseline data at ambient temperature, Structures Congress,

553   (2018) 133–144.

554 [28]. Steel Deck Institute. (C-2011). Standard for Composite Steel Floor Deck-Slabs, American

555   National Standards Institute

556 [29]. ASTM A325-14. Standard Specification for Structural Bolts, Steel, Heat Treated, 105 ksi

557   Minimum Tensile Strength. (2015) 1–8. doi:10.1520/A0325-14.2. American Society of

558   Testing and Materials, West Conshohocken, PA.

559 [30]. ASTM A36/A36M-05. Standard Specification for Carbon Structural Steel, Standards. 14

560 (2005) 1–4. doi:10.1520/A0036. American Society of Testing and Materials, West

561 Conshohocken, PA.

562 [31]. ASTM A185/A185M-07. Standard Specification for Steel Welded Wire Reinforcement

563 Plain Concrete, (2005) 1–6. doi:10.1520/A0185.

564 [32]. ASTM A29/A29M. Standard Specification for Steel Bars , Carbon and Alloy , Hot-Wrought,

565 Changes. i (2015) 1–16. doi:10.1520/A0029. American Society for Testing and Materials,

566 West Conshohocken, PA.

567 [33]. ASTM A615. Standard Specification for Deformed and Plain Billet-Steel Carbon Steel

568 Bars, (2015) 1–8. doi:10.1520/A0615. American Society of Testing and Materials, West

569 Conshohocken, PA.

570 [34]. ASTM A992/A992M-11. Standard Specification for Structural Steel Shapes,

571 doi:10.1520/A0992, American Society of Testing and Materials, West Conshohocken, PA.

572 [35]. ASTM C143/C143M. Standard Test Method for Slump of Hydraulic-Cement Concrete.

573 American Society of Testing and Materials, West Conshohocken, PA.

574 [36]. ASTM C39/C39M. Standard Test Method for Compressive Strength of Cylindrical

575 Concrete Specimens. American Society of Testing and Materials, West Conshohocken,

576 PA.

577 [37]. ASTM C642. Standard Test Method for Density, Absorption, and Voids in Hardened

578 Concrete. American Society of Testing and Materials, West Conshohocken, PA.

579 [38]. G.Q. Li, N. Zhang, J. Jiang, Experimental investigation on thermal and mechanical

580 behaviour of composite floors exposed to standard fire, Fire Saf. J. 89 (2017) 63–76.

581 doi:10.1016/j.firesaf.2017.02.009.

582

583

584

585

Table 1 Longitudinal distributed fiber optic sensor (DFOS) and thermocouple (TC) temperature readings and their relative difference (Rel. Diff.)

Specimen	CB-DA				CB-DA-SC			
Location	Top		Bottom		Top		Bottom	
Parameter	DFOS/TC (℃)	Rel. Diff.	DFOS/TC (℃)	Rel. Diff.	DFOS/TC (℃)	Rel. Diff.	DFOS/TC (℃)	Rel. Diff.
20 min after the ignition of fire								
Average		**8%**		**10%**		**17%**		**15%**
Maximum	21/23	**9%**	27/24	**13%**	33/64	48%	35/72	51%
Minimum	21/22	**5%**	23/22	**5%**	23/23	**0%**	24/24	**0%**
40 min after the ignition of fire								
Average		51%		87%		**11%**		57%
Maximum	83/25	232%	111/36	208%	32/26	23%	82/34	141%
Minimum	26/24	**8%**	30/35	**14%**	26/27	**4%**	42/41	**2%**
70 min after the ignition of fire								
Average		22%		**15%**		36%		31%
Maximum	81/48	68%	95/75	27%	81/46	76%	119/74	60%
Minimum	44/44	**0%**	70/65	**8%**	73/83	**12%**	77/87	**11%**
90 min after the ignition of fire								
Average		**18%**		**13%**		35%		40%
Maximum	102/64	59%	102/79	29%	153/89	72%	206/97	112%
Minimum	62/63	**2%**	103/97	**6%**	79/73	**9%**	109/101	**8%**
120 min after the ignition of fire								
Average		26%		**10%**		39%		59%
Maximum	107/75	43%	112/96	**17%**	224/98	129%	258/112	130%
Minimum	93/95	**2%**	94/96	**2%**	94/92	**2%**	144/118	22%

Note: The Rel. Diff. value was calculated as IDFOS-TCI / TC x 100%. The minimum, average, and maximum values were determined from six TC readings for CB-DA (Sections 4 & 6 excluded) and six TC readings for CB-DA-SC (Sections 1 & 8 excluded) at the height of the DFOS. The maximum value represents the largest error among all individual sections in each specimen. Its corresponding temperatures are given.

592

593

594

Table 2 Transverse distributed fiber optic sensor (DFOS) and thermocouple (TC) temperature readings and their relative difference (Rel. Diff.)

Specimen	CB-DA		CB-DA-SC	
Parameter	DFOS/TC (℃)	Rel. Diff.	DFOS/TC (℃)	Rel. Diff.
North Line				
Average		**17%**		29%
Maximum	159/108	47%	182/118	54%
Minimum	121/120	**1%**	120/127	**6%**
Center Line				
Average		29%		33%
Maximum	31/67	54%	139/78	78%
Minimum	52/62	**16%**	96/89	**8%**
South Line				
Average		**19%**		35%
Maximum	74/113	35%	185/116	59%
Minimum	150/139	**8%**	151/132	**14%**

Note: The Rel. Diff. value was calculated as |DFOS-TC| / TC x 100%. The minimum, average, and maximum values were determined from all TC readings for CB-DA (Sections 4 & 6 excluded at Center Line) and CB-DA-SC (Sections 1 & 8 excluded at Center Line) at 41 mm from the top surface of concrete. The maximum value represents the largest error among all individual sections in each specimen.

601

602

603

604   (a)   (b)
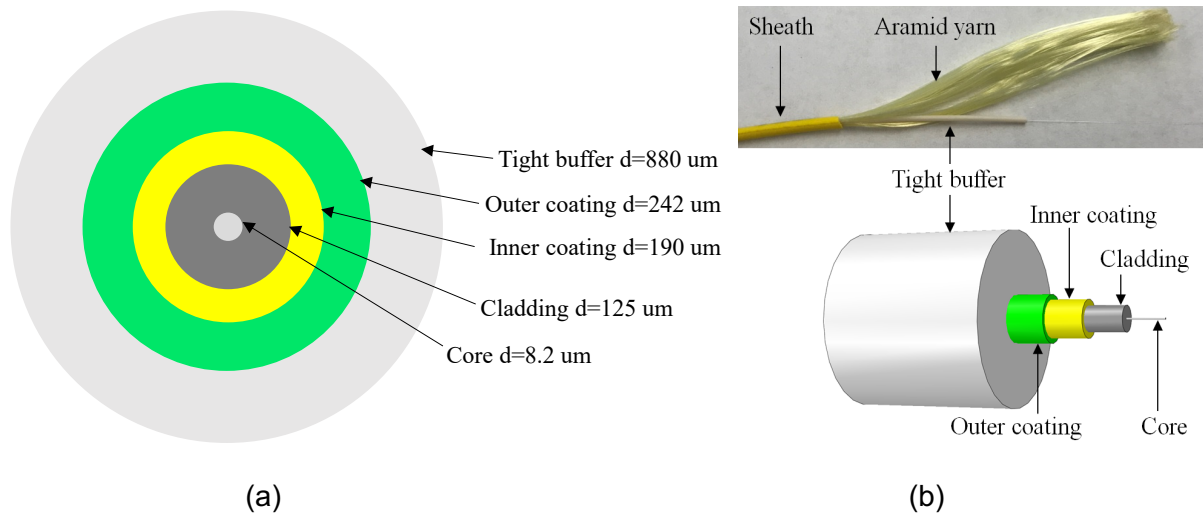
Figure 1 Single-mode optical fiber used as temperature sensors: (a) overall composition
excluding the aramid yarn and sheath and (b) photo of cross section with annotation (not to
scale)

609
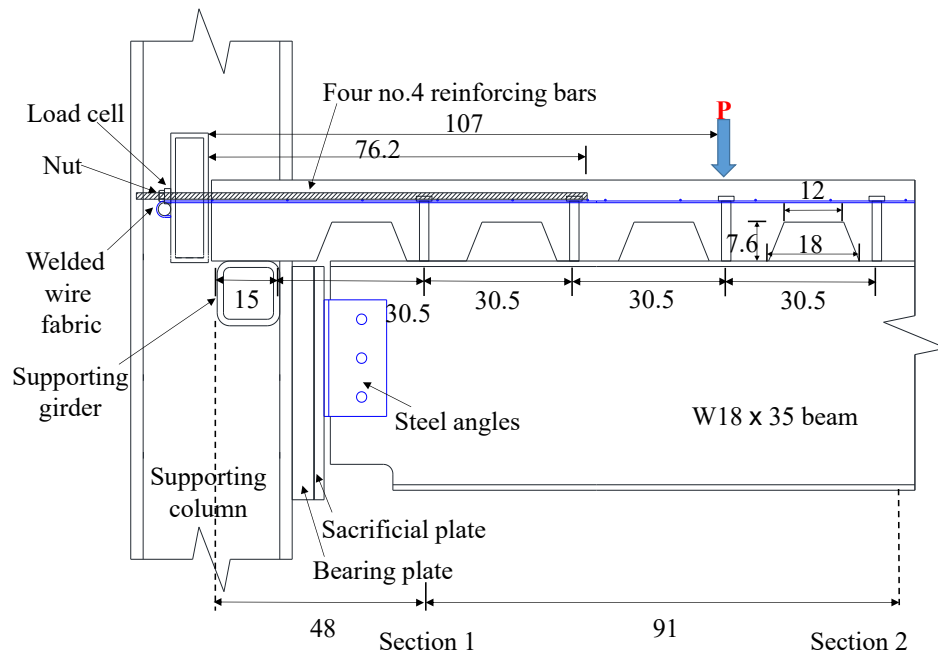
610

611 (a)
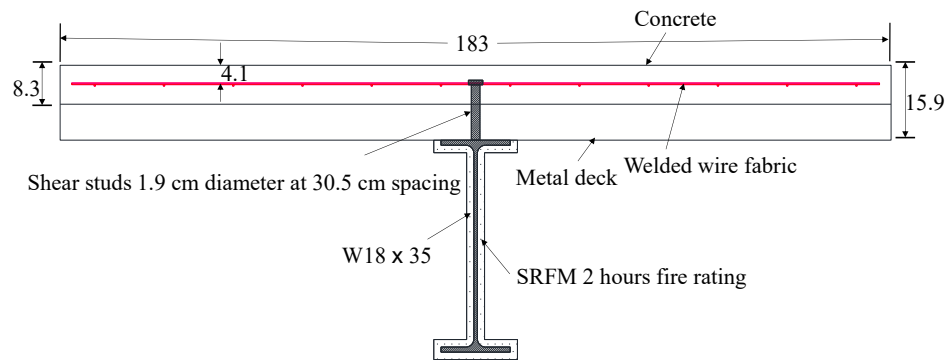
612

613 (b)

614 Figure 2 Scale drawings of (a) the specimen-to-column connection and (b) the transverse cross-
615 section of specimens (Units: cm)
616
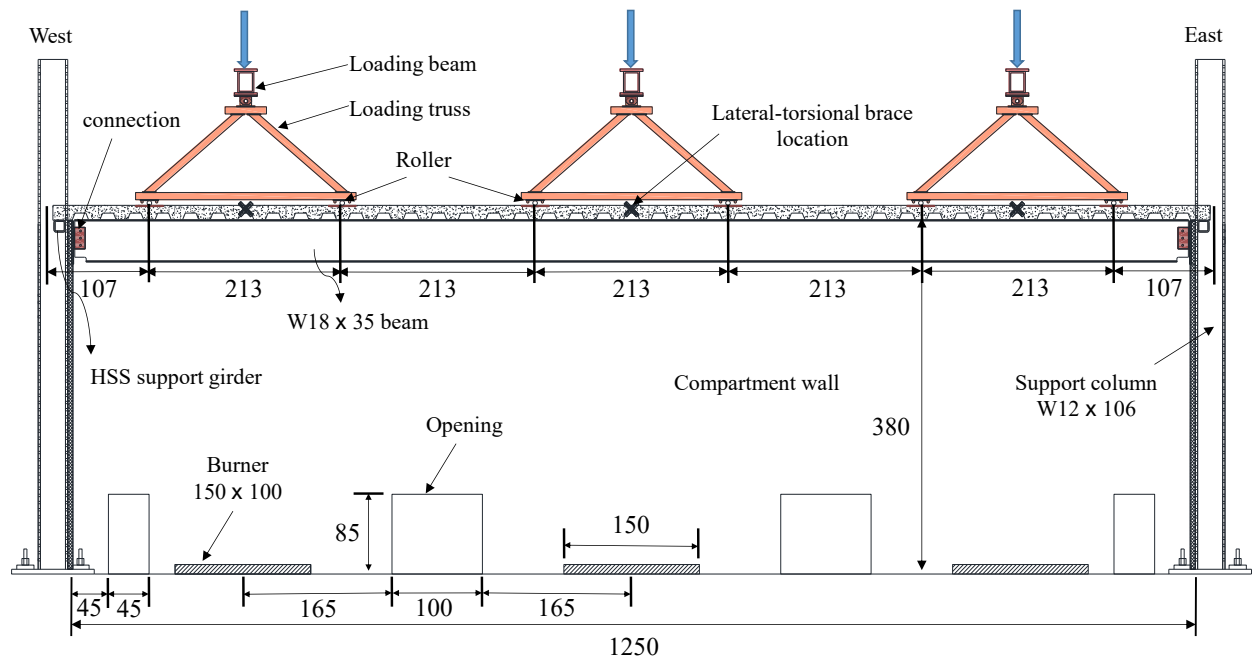
Figure 3 Scale drawing of longitudinal section of the experimental setup (Units: cm)

621

622

623 (a)

624

625 (b)
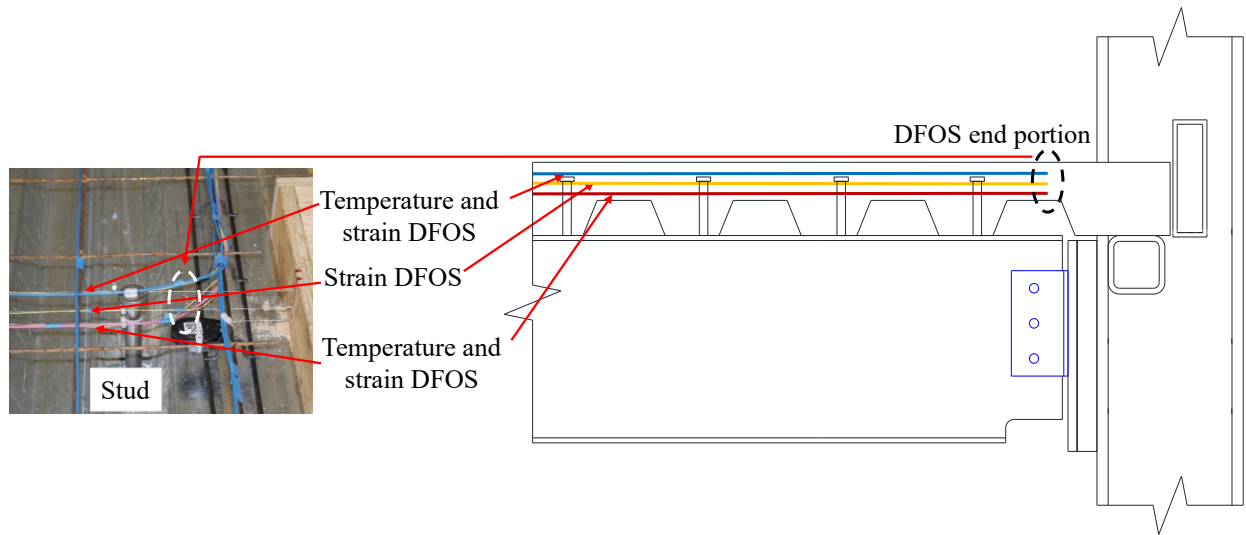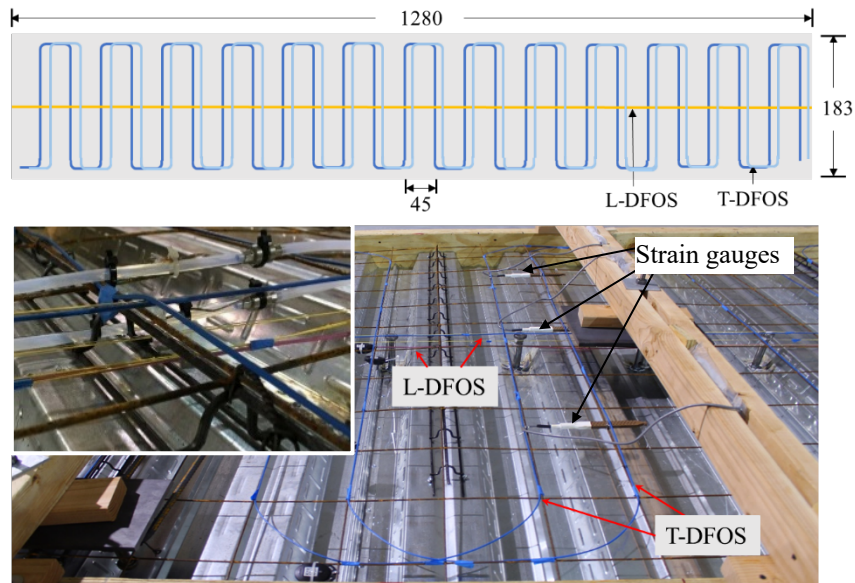
626 Figure 4 Specimen instrumentation: (a) longitudinal distributed fiber optic sensors (L-DFOS) for
627 temperature and strain and (b) transverse distributed fiber optic sensors (T-DFOS) and strain
628 gauges (Units: cm)
629

630

(a)

(b)

631
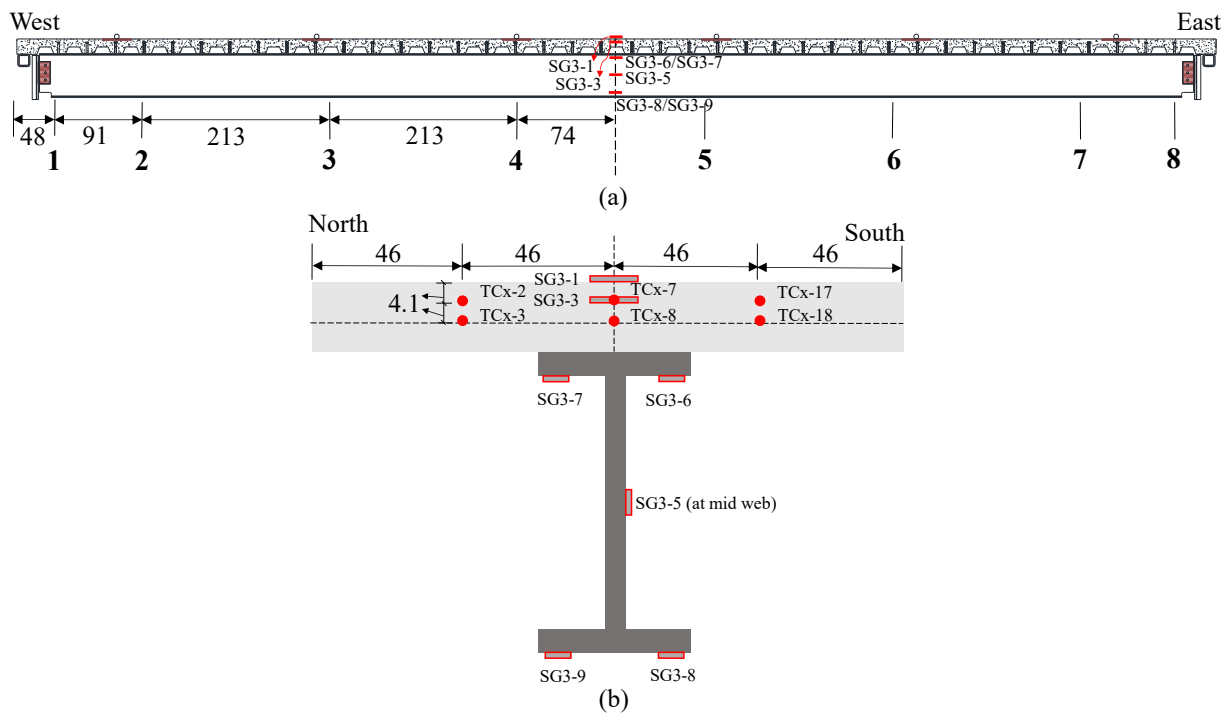
Figure 5 Locations and labels of Type K thermocouples (TC) mounted on each specimen: (a) cross section numbers (x=1 through 8) and (b) TC designations at each cross section and strain gauges (SG) at mid-span cross section (Units: cm)

635

636

637
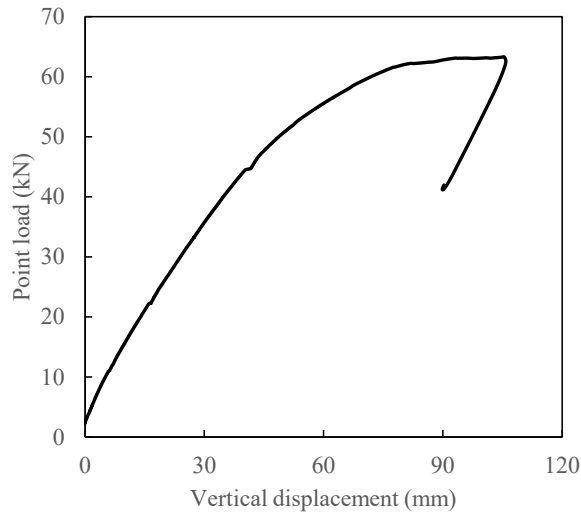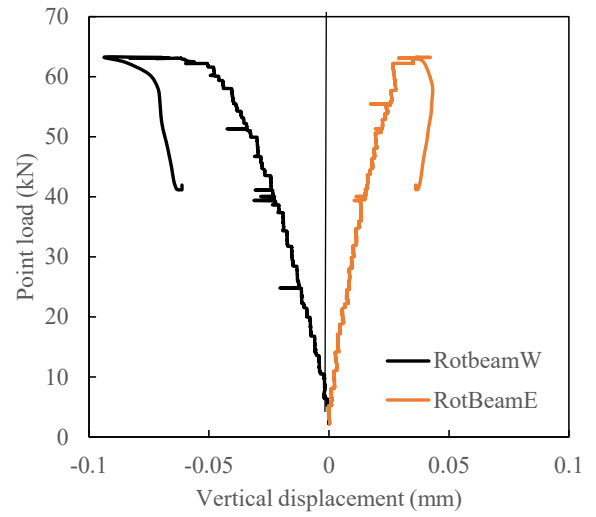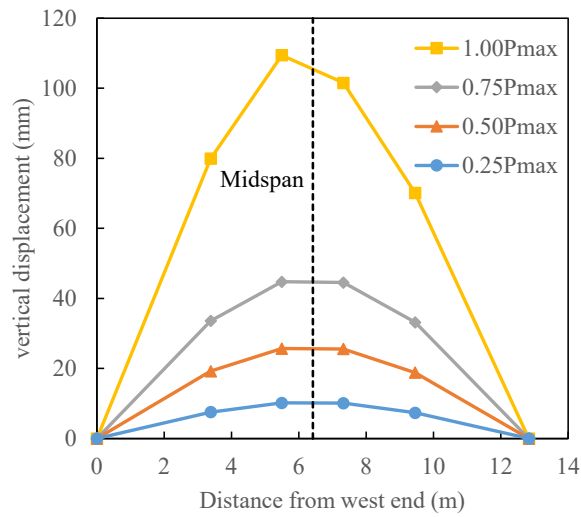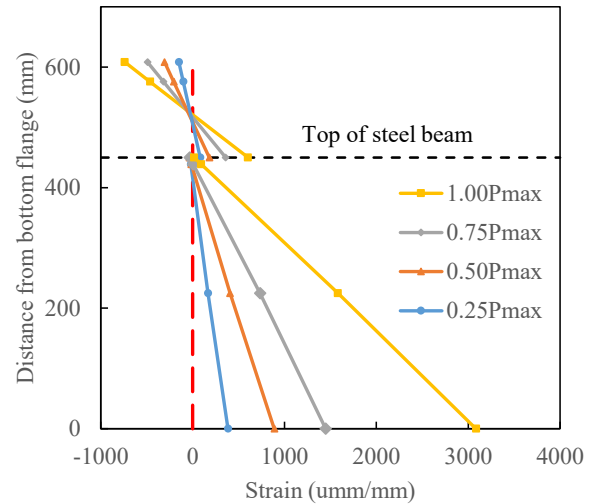
Figure 6 Test results of CB-DA-AMB specimen: (a) point load versus mid-span deflection, (b) beam rotation at two ends, (c) deflection curves, and (d) strain distribution in mid-span cross section during the first cycle of loading up to P_{max}

(a)

(b)
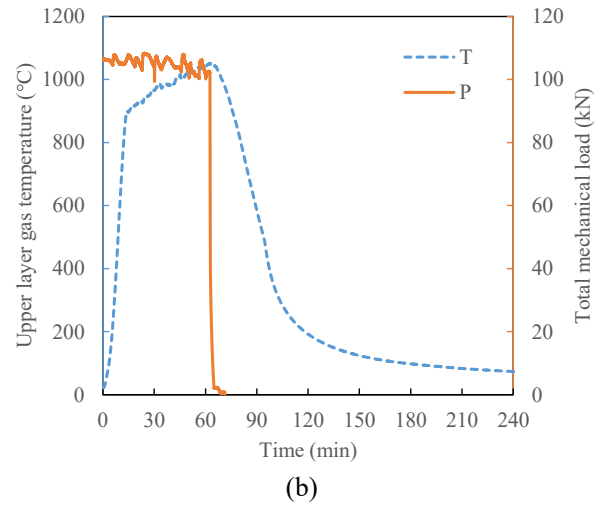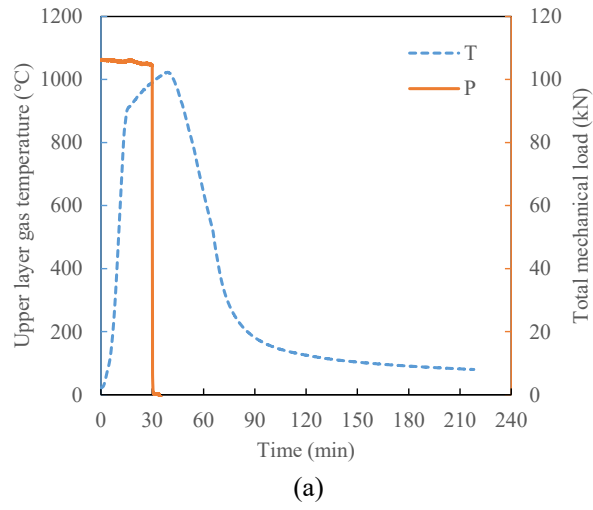
Figure 7 Gas temperature (T) measured 81 cm below concrete slab and total applied
mechanical load (P) for (a) CB-DA specimen and (b) CB-DA-SC specimen

648

(a)

(b)

(c)

649
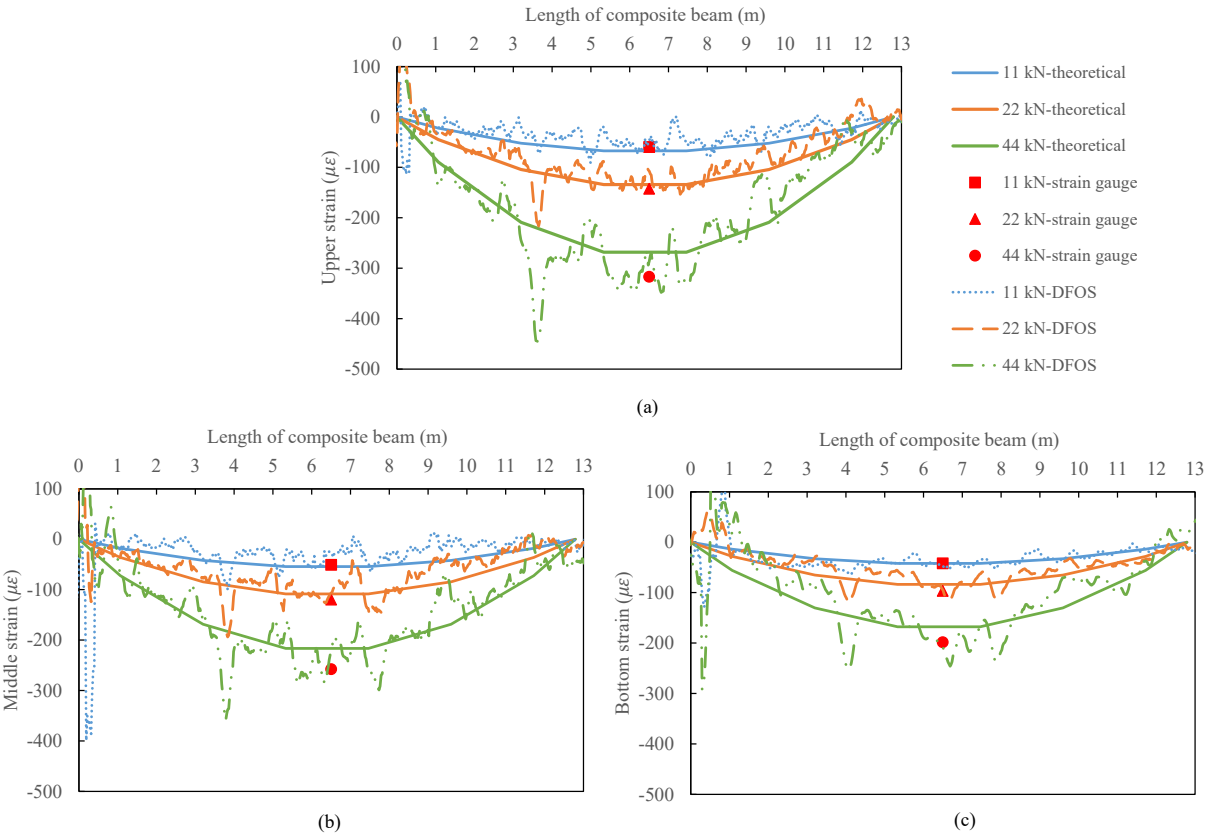
Figure 8 Strain distributions measured from the DFOS system in CB-DA-AMB at ambient
temperature along with theoretical predictions and interpolation/extrapolation from strain gauge
measurements: (a) upper, (b) middle, and (c) lower

650
651
652
653
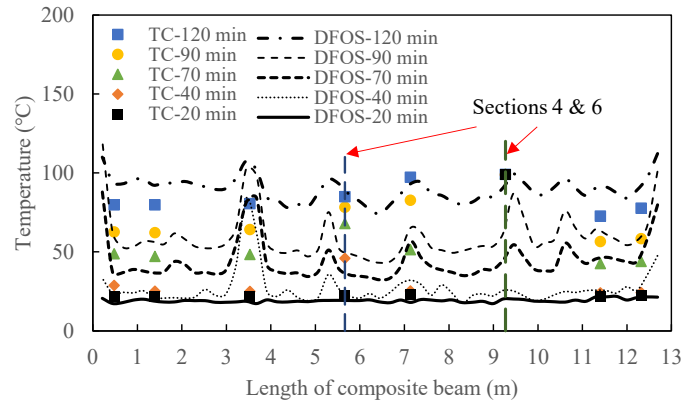
(a)
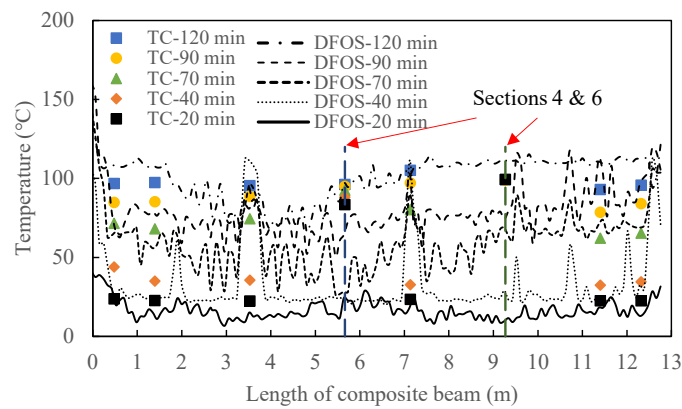
(b)
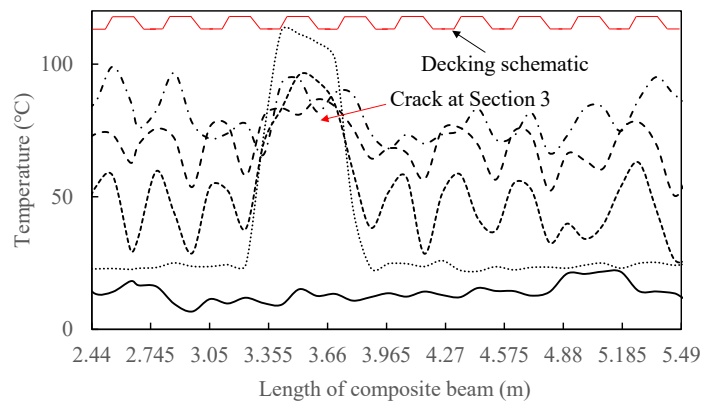
(c)

Figure 9 Concrete slab temperatures measured from thermocouple (TC) and distributed fiber optic sensors (DFOS) in CB-DA specimen at various times after fire ignition: (a) 32 mm and (b) 70 mm below the top surface of the slab, and (c) 70 mm below the top surface of the slab (between 2.44 m and 5.49 m) in (b)

34

666

(a)

669

670
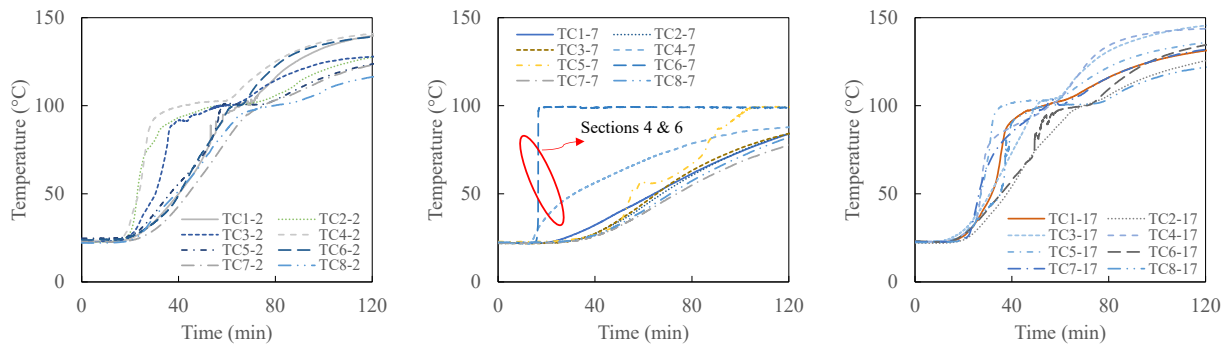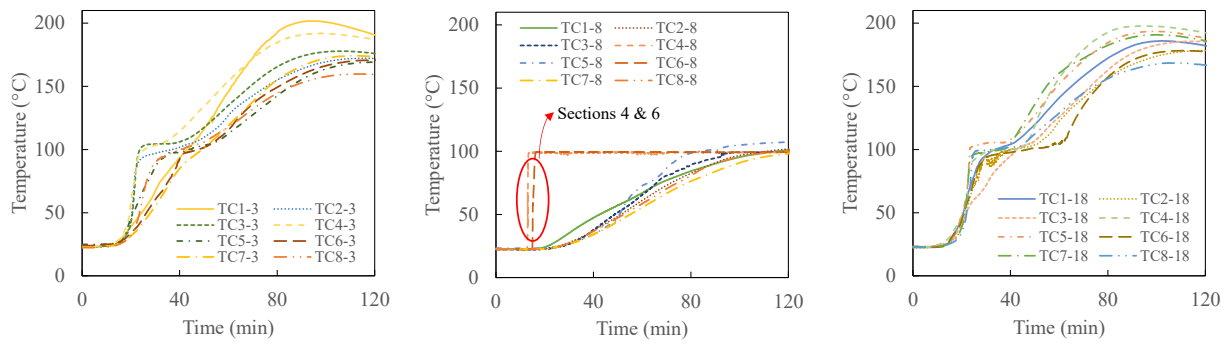
(b)

Figure 10 Concrete slab temperatures versus time measured from thermocouples (TC) in CB-DA specimen along the centerline (TCx-7 and TCx-8) and 46 cm to the north (TCx-2 and TCx-3) and south (TCx-17 and TCx-18) of the centerline at Sections 1 to 8: (a) 41 mm and (b) 82 mm below the top surface

675

676

677

678
679

(a)

680

681

(b)

682

683
684

(c)
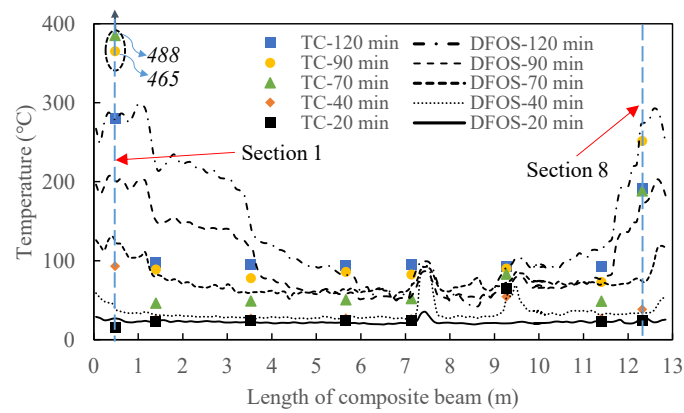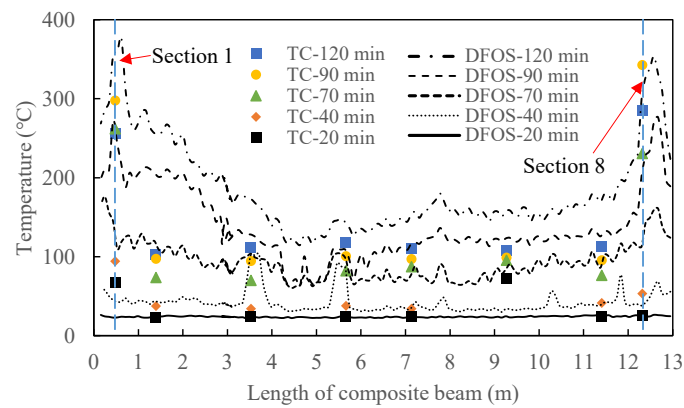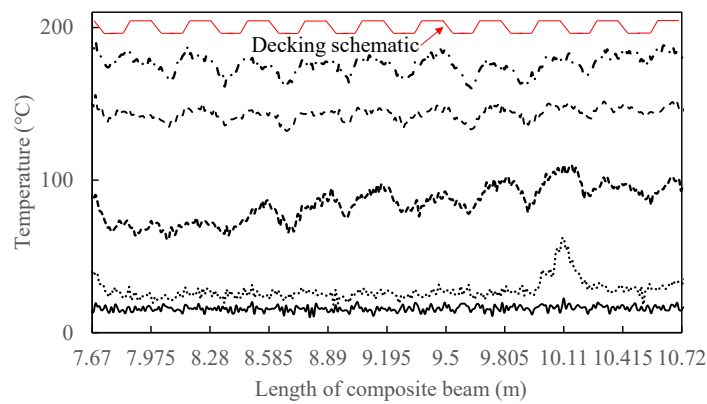
685   Figure 11 Concrete slab temperatures measured from TC and DFOS in CB-DA-SC specimen at
686   various times after fire ignition: (a) 32 mm, (b) 70 mm below the top surface, and (c) 70 mm
687   below the top surface of the slab (between 7.67 m and 10.72 m) in (b)
688

689

(a)   (b)

690
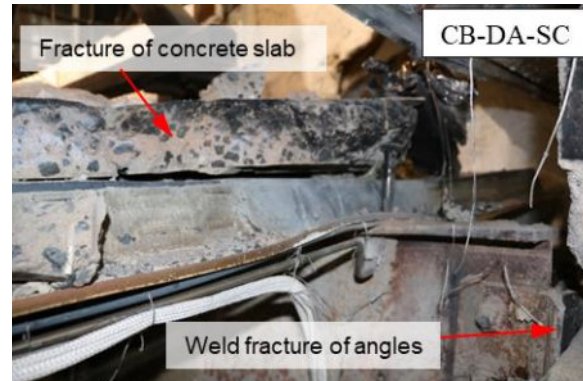
Figure 12 Photographs of damage to specimen CB-DA-SC after cool-down: (a) concrete cracks
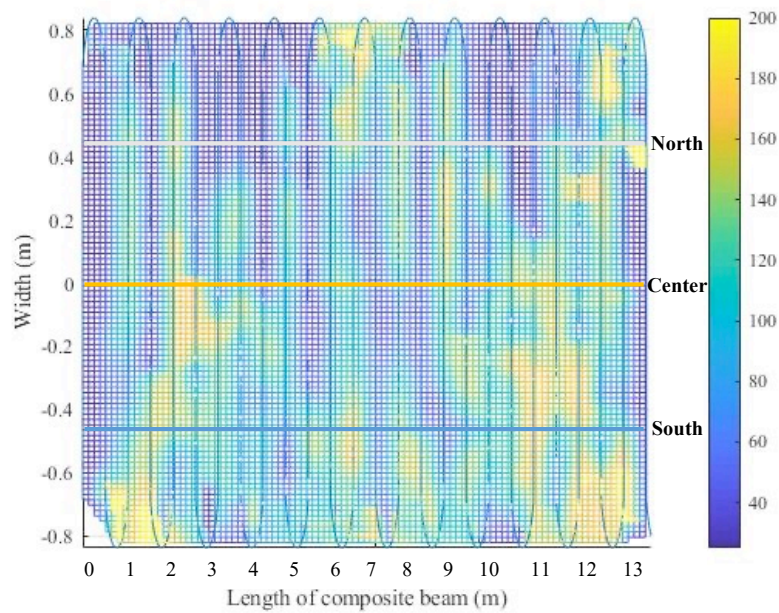(top view) and (b) fractures at east end (cross section)

693

694

695
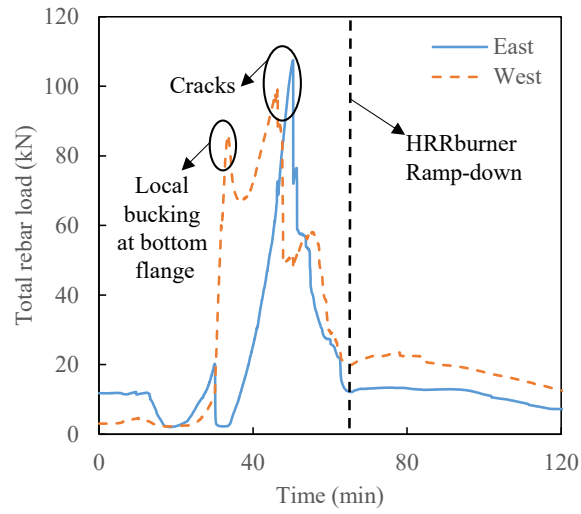
Figure 13 Total tensile loads in east and west reinforcing bars of the CB-DA-SC specimen

696
697

698

699

700

701
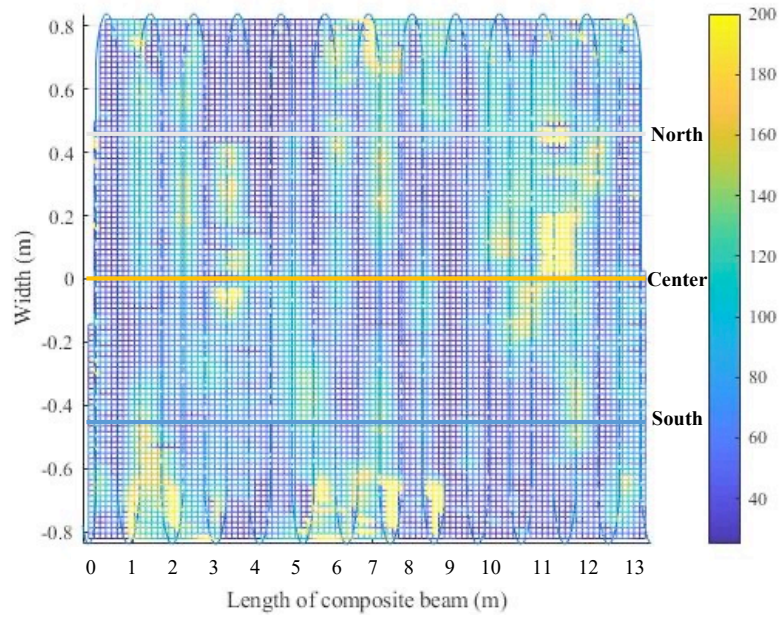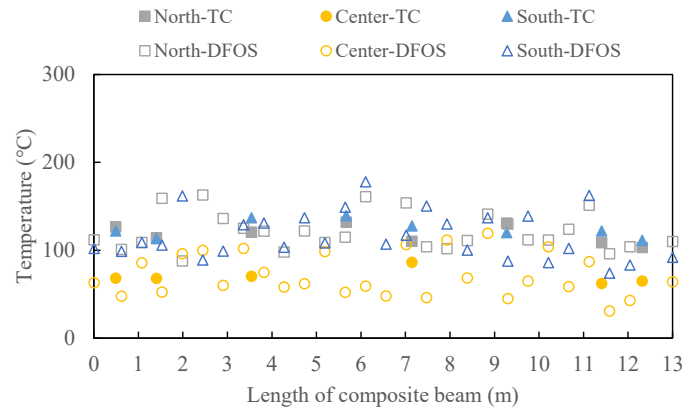

(a)

(b)

Figure 14 Transverse temperature distribution in the slab of (a) CB-DA and (b) CB-DA-SC 90 min after ignition measured from the DFOS
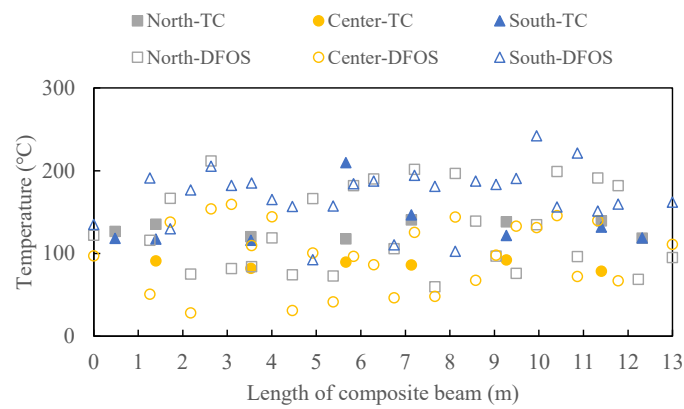
708

(a)

709

710

711

(b)

712

713

Figure 15 Transverse temperatures measured from TC and DFOS in the slab of (a) CB-DA
(b) CB-DA-SC 90 min after ignition at select locations

714
715
716